What caused the long duration of the Paleocene-Eocene Thermal Maximum?

Richard E. Zeebe

[1]   Paleorecords show that the Paleocene-Eocene Thermal Maximum (PETM, $\sim$56 Ma) was associated with a large carbon cycle anomaly and global warming >5 K, which persisted for at least 50 kyr. Conventional carbon cycle/climate models that include a single initial carbon input pulse over $\sim$10 kyr fail to reproduce the long duration of the PETM without invoking additional, slow carbon release over more than 50 kyr (hereafter referred to as bleeding). However, a potential carbon source for the bleeding, as well as its release mechanism, has hitherto remained elusive. Here I present first-principle calculations of heat transfer in marine sediments which demonstrate that a bottom water temperature anomaly as generated during the PETM takes tens of thousands of years to penetrate the top few hundred meters of deep-sea sediments. While the initial temperature rise has been suggested to cause dissociation of the majority of oceanic methane hydrate within $\sim$10 kyr, my calculations reveal a long tail of hydrate dissociation, causing smaller but continued carbon release substantially beyond 10 kyr. In addition, I suggest that temperature-enhanced metabolic processes in marine sediments and the absence of methane hydrate deposition during the PETM contributed to prolonged carbon input during the event. Enhanced fluxes of methane over this time scale would have sustained the carbon isotope excursion and amplified long-term greenhouse warming by elevating atmospheric concentrations of steady state CH_4, or in oxidized form, CO_2.

1. Introduction

[2] The Paleocene-Eocene Thermal Maximum (PETM, $\sim$56 Ma) is characterized by transient global warming >5 K, with a relatively rapid onset and a gradual recovery on a hundred-thousand-year time scale [e.g., *Kennett and Stott*, 1991; *Dickens et al.*, 1995; *Zachos et al.*, 2003, 2005, *Sluijs et al.*, 2006]. The onset was accompanied by intense dissolution of carbonate sediments throughout the deep sea as well as an anomalous excursion in the $^{13}C/^{12}C$ ratio of the surficial carbon reservoir, i.e., ocean, atmosphere, and biosphere [*Kennett and Stott*, 1991; *Koch et al.*, 1992]— phenomena which could only have been generated by a rapid and massive release of carbon. One possible source for the carbon is the release of methane from marine gas hydrate systems [*Dickens et al.*, 1995]. The released methane would have been oxidized relatively quickly to CO_2 in the water column or the atmosphere [*Schmidt and Shindell*, 2003; *Kessler et al.*, 2011; *Joye et al.*, 2011; *Carozza et al.*, 2011]. It is important to keep in mind that a pulsed, as well as a

continued carbon release from methane hydrate dissociation during the PETM would have acted as a feedback to some initial warming, rather than the trigger of the event. For a detailed discussion of the methane hydrate hypothesis and alternative scenarios including other potential carbon sources, see *Dickens* [2011].

[3] Regardless of the age model applied to determine the chronology of the event (i.e., orbital stratigraphy and ^{3}He abundance), the PETM main phase seems to have lasted for at least 50 kyr [*Röhl et al.*, 2007; *Farley and Eltgroth*, 2003; *Murphy et al.*, 2010; *Charles et al.*, 2011; *Zeebe and Zachos*, 2013]. This is reflected in stable carbon and oxygen isotope records, Mg/Ca ratios but also in B/Ca ratios of planktic foraminifera, indicating prolonged changes in surface ocean temperature and carbonate chemistry [*Penman et al.*, 2011]. To explain the long duration of the PETM, *Zeebe et al.* [2009] made an *ad hoc* assumption invoking additional, continued carbon release of 1500 Pg C over > 50 kyr (here referred to as bleeding) after the initial carbon input pulse of 3000 Pg C. Note that in order to be consistent with carbon isotope records and transient dissolution patterns, *Zeebe et al.* [2009] required the isotopic composition of the source carbon for the bleeding to be lighter than –50‰. Understanding the mechanisms behind the long duration of the PETM is important for at least two reasons. First, identifying the mechanisms will advance our fundamental understanding of carbon cycle-climate feedbacks in the

School of Ocean and Earth Science and Technology, University of Hawaii at Manoa, Honolulu, Hawaii 96822, USA.

Corresponding author: R. E. Zeebe, School of Ocean and Earth Science and Technology, University of Hawaii at Manoa, 1000 Pope Rd., MSB 629, Honolulu, HI 96822, USA. (zeebe@hawaii.edu)

Earth system. Second, it is critical to determine whether such mechanisms are applicable to the long-term future warming due to greenhouse gas release from anthropogenic sources. If the answer is yes, then the lifetime of human-induced warming will be much longer than previously thought.

[4] Here I examine possible mechanisms that may have caused the bleeding, mainly focusing on slow release of hydrates in subsurface sediments as a result of slow penetration of the temperature anomaly generated at the sediment-water interface (SWI) into the deeper layers of the sediment column. The problem can be studied using the well-known theory of heat conduction. First, I show that a simple scale analysis gives the perhaps surprising result that it takes tens of thousands of years for the temperature anomaly to penetrate the top few hundred meters of sediment. I also show that advection can be safely ignored in the analysis. Next, some analytical solutions for the temporal evolution of the temperature profile are given (one exact and one approximate solution during different time intervals). The full problem is then solved numerically including the complete time-dependent forcing of temperature changes at the SWI and latent heat uptake from hydrate dissociation. The consequences for long-term carbon bleeding during the PETM are examined in the discussion. Finally, additional processes that may have contributed to the prolonged carbon input are discussed, including temperature-enhanced metabolic processes in marine sediments and the absence of methane hydrate deposition during the warmth of the PETM.

2. Theory

[5] The heat transfer equation in one dimension in a simple medium (constant density and thermal properties, no advection, no internal heat sinks/sources, etc.) may be written as:

$$\rho \, C_p \frac{\partial T}{\partial t} = \mathcal{K} \frac{\partial^2 T}{\partial z^2} , \qquad (1)$$

where ρ, C_p, and $\mathcal{K}$ are the density, specific heat, and thermal conductivity of the medium; z is the vertical coordinate (e.g., depth below seafloor, positive downward; below, $z = 0$ refers to the sediment-water interface). Dividing by $\rho \, C_p$ yields

$$\frac{\partial T}{\partial t} = \kappa \frac{\partial^2 T}{\partial z^2} , \qquad (2)$$

where $\kappa = \mathcal{K}/(\rho \, C_p)$ is the thermal diffusivity. Typical values for the thermal parameters in marine sediments are $\mathcal{K} \simeq 1.0$ W m^{-1} K^{-1}, $\rho \, C_p \simeq 3.3 \times 10^6$ J m^{-3} K^{-1}, and $\kappa \simeq 3.0 \times 10^{-7}$ m^2 s^{-1} [e.g., *Von Herzen and Maxwell*, 1959; *Morin and von Herzen*, 1986; *Dickens et al.*, 1995; *Rempel and Buffett*, 1997]. For heat transfer in deep-sea sediments, we may write the temperature profile as

$$T = T_{\text{eq}} + \mathcal{T} = G_0 z + \mathcal{T} , \qquad (3)$$

where $G_0 \simeq 0.03 - 0.05$ K m^{-1} is the initial geothermal gradient, $T_{\text{eq}} = G_0 z$ is the initial steady state profile prior to temperature perturbation, and $\mathcal{T}$ is the temperature anomaly. Inserting into equation (2) gives

$$\frac{\partial \mathcal{T}}{\partial t} = \kappa \frac{\partial^2 \mathcal{T}}{\partial z^2} . \qquad (4)$$

Hence, we can solve the same equation for the temperature anomaly as for the full profile.

2.1. Characteristic Time Scale of Heat Transfer

[6] For the semi-infinite solid (linear geometry), the characteristic time scale of heat transfer can be written as [*Carslaw and Jaeger*, 1959]:

$$\tau = \frac{h^2}{\kappa} , \qquad (5)$$

where h is a typical length scale and κ is the thermal diffusivity. Note that τ is hence proportional to the square of h. Using $\kappa \simeq 3 \times 10^{-7}$ m^2 s^{-1} = 9.5 m^2 y^{-1} for deep-sea sediments, the time for a temperature anomaly generated at the sediment-water interface to reach a sediment depth of 100 and 500 m is $\sim$1 and $\sim$26 kyr, respectively. Allowing a $\pm$20% uncertainty in κ, τ ranges from 0.9 to 1.3 ky and 22 to 33 kyr, respectively. This simple scale analysis shows that it takes tens of thousands of years for a temperature anomaly to penetrate the top 500 m of sediment. This result could have been inferred from earlier studies [e.g., *Xu et al.*, 2001; *Katz et al.*, 2001]. However, *Katz et al.* [2001], for instance, modeled only the first 10 kyr following the onset of the PETM. Neither of the studies above focused on the long tail of methane hydrate dissociation as a result of the slow heat propagation.

2.2. The Role of Diffusion and Advection

[7] The heat transfer equation including diffusion and advection for the full temperature profile may be written as

$$\frac{\partial T}{\partial t} = \kappa \frac{\partial^2 T}{\partial z^2} - w \frac{\partial T}{\partial z} , \qquad (6)$$

where w is the advection velocity. The relative importance of diffusion and advection may be evaluated in steady state:

$$\frac{\partial^2 T}{\partial z^2} = \frac{w}{\kappa} \frac{\partial T}{\partial z} . \qquad (7)$$

Using equation (3), the solution to equation (7) is (Appendix A):

$$T = T_0 + G_0 h (e^{wz/\kappa} - 1)/(e^{wh/\kappa} - 1) , \qquad (8)$$

where $T_0 = T(z = 0)$ and h is the base of the geotherm. For typical values of $w = 1 \times 10^{-4}$ m y^{-1} [*Richter*, 1993; *Adkins and Schrag*, 2003; *Fantle and DePaolo*, 2006] and $\kappa = 9.5$ m^2 y^{-1}, $w/\kappa \simeq 1 \times 10^{-5}$ m^{-1}. Using $h = 100 - 1000$ m, $w \times h/\kappa \simeq 0.001 - 0.01$. Hence, we can use $e^x \simeq 1 + x$, the ratio on the right-hand side becomes z/h, and the solution is essentially a straight line:

$$T \simeq T_0 + G_0 z , \qquad (9)$$

which is the solution for pure diffusion. Thus, advection can be neglected to a very good approximation for the present purpose.

2.3. Temperature Forcing and Boundary Conditions

[8] During the onset of the PETM, ocean bottom waters warmed by $\sim$5 K over a few thousand years [*Dickens et al.*, 1995; *Zachos et al.*, 2001; *Bice and Marotzke*, 2002; *Tripati and Elderfield*, 2005]. Furthermore, independent age models suggest that the duration of the PETM main phase of globally elevated temperatures exceeded 50 kyr [*Röhl et al.*, 2007; *Farley and Eltgroth*, 2003; *Murphy et al.*, 2010;
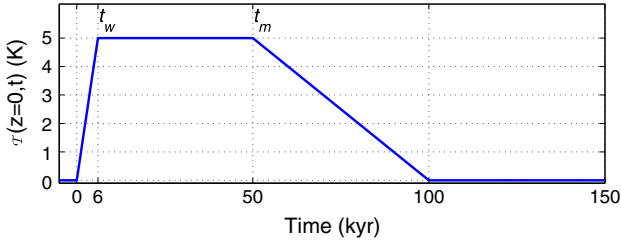
Figure 1. Prescribed temperature forcing (anomaly) at the sediment-water interface (SWI, $z = 0$). The end of the initial warming phase is indicated by t_w and the main phase duration by t_m. Note that 50 kyr for the duration of the main phase temperature anomaly is a lower limit.

Charles et al., 2011; *Zeebe and Zachos*, 2013]. These observations were used to construct the temperature forcing at the top of the model domain (Figure 1). Note that in reality, a potential carbon release from methane hydrate dissociation would have acted as a feedback to some initial warming. However, this feedback is not part of the current model—the temperature forcing is simply prescribed. A model with a fully interactive feedback would be substantially more complex (see section 6.8). At the sediment-water interface ($z = 0$), the temperature boundary condition $T(t, 0)$ is provided by the temporal evolution of the bottom water temperature $T_b(t)$, i.e., $T(t, 0) = T_b(t)$.

[9] At the base of the model domain ($z = h$), a flux boundary condition is imposed such that the geothermal heat flux from below (in W m^{-2}) is constant over the time scale considered. That is, $\mathcal{K} \, \partial T/\partial z|_{z=h} = \mathcal{K} \, G_0$, or $\partial \mathcal{T}/\partial z|_{z=h} = 0$ (see equation (3)). On a time scale of 10^5 y, a heat flux anomaly generated at the sediment-water interface can diffuse to a depth of about 1 km below seafloor. The vertical length scale h used in the calculations hence needs to be of the same order—otherwise, if h is too small, imposing $\partial \mathcal{T}/\partial z = 0$ at a shallow sediment depth would artificially dampen the heat flux anomaly. Yet, a large value of h may slightly complicate the calculations because the base of the vertical model domain may extend beyond the sediment-basement interface.

[10] Methane hydrate reservoirs preferentially form on continental margins, where the sediment thickness often exceeds 2 km on passive margins [*Divins*, 2003]. Hence in many typical target areas, the lower model boundary is located within the sediment section. On active margins, however, the sediment thickness may only be of order ∼500 m. Calculating temperature profiles across hydrate reservoirs in those areas over time scales of 10^5 y therefore should consider that the lower boundary may have to be located in the basement underlying the sediment. The basement is generally composed of basalt with thermal properties that potentially differ from those of the sediment, which would require a depth-dependent thermal diffusivity to be included in the calculations. However, as it turns out, the thermal properties of e.g., carbonate sediments and basalt at a few kilometer depth below the seafloor are not significantly different.

[11] The difference in thermal properties between e.g., two mineral-water phases depends primarily on (i) the bulk porosity (ϕ) and (ii) the density (ρ_m), specific heat (C_m),

and thermal conductivity ($\mathcal{K}_m$) of the mineral. For instance, typical values for limestone/basalt (at low mineral porosities) are ρ_m = 2600/2900 kg m^{-3}, C_m = 1000/1000 J kg^{-1} K^{-1}, and $\mathcal{K}_m$ = 2.5–3.0/1.8–2.6 W m^{-1} K^{-1} [e.g., *Robertson*, 1988; *Vosteen and Schellschmidt*, 2003]. Typical bulk porosities of carbonate sediments and basalt at $1 - 2$ km below seafloor are ϕ = 0.25 – 0.40 and ϕ = 0.10 – 0.25, respectively [*Goldhammer*, 1997; *Carlson and Herrick*, 1990]. These properties are quite similar, except for $\mathcal{K}_m$ and ϕ being slightly lower in the basalt mineral and the basalt-pore fluid phase, respectively. Hence, the slightly lower thermal conductivity in the basalt mineral is partly compensated for by the slightly lower bulk porosity of the basalt-pore fluid phase (the thermal conductivity of the mineral being higher than that of the pore fluid). For example, the bulk $\kappa = \mathcal{K}/(\rho \, C_p)$ may be estimated using

$$\rho \, C_p = \rho_w \, C_w \, \phi + \rho_m \, C_m (1 - \phi) \,, \qquad (10)$$

where indices w and m refer to seawater and mineral, respectively. Using values for ρ_m and C_m as given above, and $\mathcal{K}_m$ = 1.5 and 1.6 W m^{-1} K^{-1} at ϕ = 0.40 and 0.25 for carbonate sediment and basalt, respectively [*Robertson*, 1988], the bulk κ for carbonate sediment and basalt differs by only ∼6%. As a result, potential changes in the thermal diffusivity in the bottom kilometer or so of the sediment-basement section were neglected in this study. In other words, a constant, depth-invariant κ was assumed.

2.4. Latent Heat Uptake From Hydrate Dissociation

[12] Hydrate dissociation requires uptake of latent heat, which may affect the evolution of the temperature profile and hence the total amount of hydrate dissociation and/or the timing of the dissociation at certain sediment depths. Latent heat uptake could effectively delay warming of adjacent subsurface sediments and thus delay the release of CH$_4$ from those sections. On the time scales considered here ($10^3 - 10^5$ y), the latent heat associated with the phase transition of methane hydrate dissociation has been neglected in earlier studies [*Dickens et al.*, 1995; *Xu et al.*, 2001]. However, a simple estimate suggests that latent heat uptake can be significant.

[13] The latent heat uptake per unit volume of sediment may be estimated as

$$Q_H = c_H \, L_H \,, \qquad (11)$$

where c_h is the hydrate concentration per total sediment volume (kg m^{-3}) and L_H = 430×10^3 J kg^{-1} is the latent heat of methane hydrate formation/dissociation [*Rempel and Buffett*, 1997]. The hydrate concentration c_H may be obtained from the hydrate pore space fraction f_H using

$$c_H = f_H \, \phi \, \rho_H \,, \qquad (12)$$

where ϕ is the bulk porosity and ρ_H = 930 kg m^{-3} is the density of methane hydrate. Hence:

$$Q_H = f_H \, \phi \, \rho_H \, L_H \,. \qquad (13)$$

Dividing by the bulk density ρ and specific heat C_p gives a temperature change

$$\mathcal{T}_H = Q_H \, (\rho \, C_p)^{-1} = f_H \, \phi \, \rho_H \, L_H \, (\rho \, C_p)^{-1} \,. \qquad (14)$$

For instance, using f_H = 0.05, ϕ = 0.5, and $\rho \, C_p$ = 3.3 × 10^6 J m^{-3} K^{-1} gives $\mathcal{T}_H$ = 3 K. In other words, without
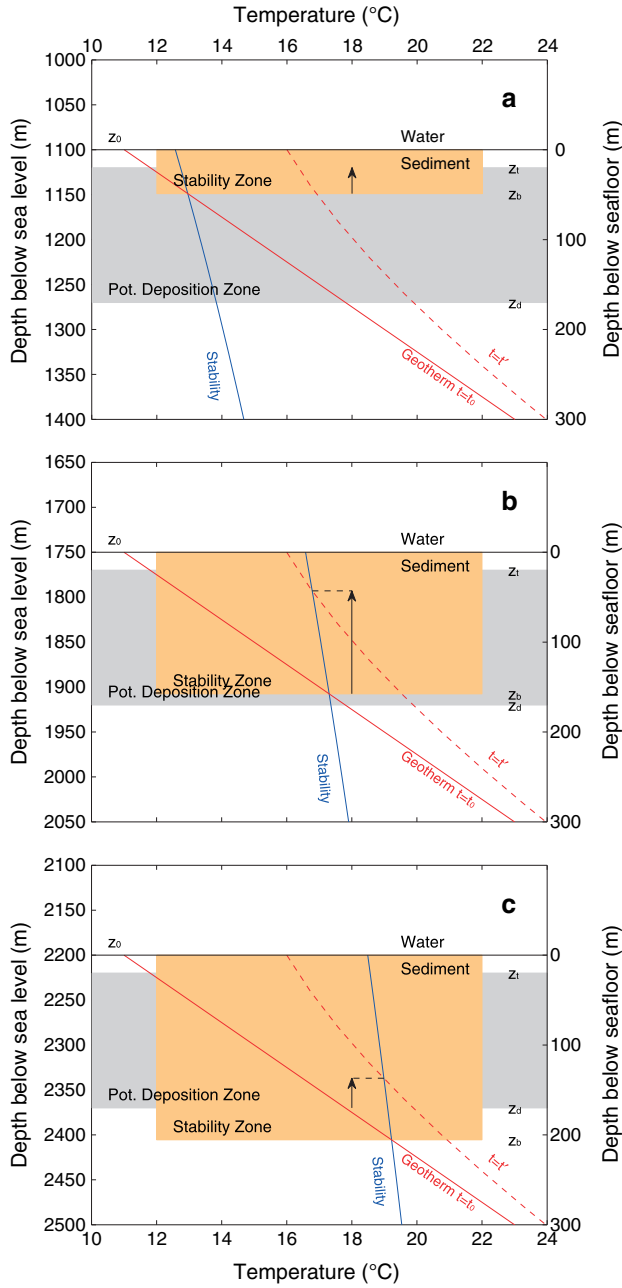
Figure 2. Schematic illustration of methane hydrate dissociation in sediments at different depths below sea level: (a) 1100 m, (b) 1750 m, (c) 2200 m [cf. *Dickens et al.*, 1995]. Methane hydrates become unstable at temperatures exceeding those indicated by the blue stability curve. The stability base (z_b) is located where the geotherm and the stability curve intersect (orange shaded area: stability zone). z_t and z_d: top and base of potential deposition zone (grey shaded areas). Geotherm at the beginning ($t_0 = 0$ kyr) and end ($t' = 6$ kyr) of initial warming phase (solid and dashed red line). Arrows indicate the layer of hydrate dissociation between t_0 and t'.

heat transfer, latent heat uptake would cool 1 m³ of sediment by 3 K—a significant temperature change relative to a bottom water warming of say 5 K. The thermal effect of hydrate dissociation was included in the numerical model by adding a latent heat term to the heat transfer equation (see section (3.3)):

$$\frac{\partial T}{\partial t} = \kappa \frac{\partial^2 T}{\partial z^2} - q_H \,, \tag{15}$$

with

$$\begin{array}{ll} q_H = Q_H \, (\rho \, C_p \, \Delta t_d)^{-1} & \text{if } t = t_{hd}(z) \\ q_H = 0 & \text{else} \,, \end{array} \tag{16}$$

where the hydrate dissociation time ($t_{hd}(z)$) is the time when the temperature at depth z (within the hydrate layer) exceeds the methane hydrate dissociation temperature (see below); Δt_d is the dissociation time interval during which the latent heat is taken up (numerically, Δt_d may be taken equal to the time step Δt). To avoid numerical instabilities, the latent heat uptake during hydrate dissociation at a single model grid point was distributed over several grid points and time steps.

2.5. Hydrate Stability Zone and Dissociation Flux at Various Depths

[14] The dissociation temperature of methane hydrate (in °C) in seawater is given by

$$T_d(\mathcal{Z}) = a + b \cdot \log(\mathcal{Z}/1000) - c \cdot [\log(\mathcal{Z}/1000)]^2 \,, \tag{17}$$

where $\mathcal{Z}$ is depth in m below sea level (mbsl), $a = 11.726$, $b = 20.5$, and $c = 2.2$ [*Dickens and Quinby-Hunt*, 1994; *Brown et al.*, 1996]. Within the zone between $T_d(\mathcal{Z})$ and the geotherm, methane hydrate is stable (Figure 2). However, within this zone, hydrates of course only exist where deposited (usually not directly below the SWI). Thus, the following calculations use a potential deposition zone in which hydrates may theoretically be deposited, here taken as a 150 m thick layer extending from 20 mbsf to 170 mbsf (see below). However, the zone where methane hydrates actually occur in sediments is restricted to the overlap of the zones of stability and potential deposition (Figure 2).

[15] Let the top and base of the potential deposition zone be z_t and z_d and the base of the stability zone be z_b (lowercase z's measure depth in m below seafloor, mbsf, Figure 2). In the case when the stability base lies within the potential deposition zone ($z_t < z_b < z_d$), the hydrate inventory m_H at a given seafloor depth z_0 may be written as $m_H(z_0) = \{a_H \, c_H \, (z_b - z_t)\}_{z_0}$, where a_H is the area containing hydrates at seafloor depth z_0 and c_H its concentration (e.g., in units of g C m⁻³). Obviously, if the top of the potential deposition zone lies below the stability base ($z_t > z_b$), hydrates cannot exist and $m_H = 0$ (set $z_b = z_t$). If the deposition base lies above the stability base ($z_d < z_b$, Figure 2c), hydrates could exist above z_b but would not occur due to a lack of deposition in that zone (set $z_b = z_d$). Thus, the hydrate inventory at a given seafloor depth z_0 can be expressed as

$$m_H(z_0) = \{a_H \, c_H \, (z_b - z_t)\}_{z_0} \quad \begin{array}{l} \text{if } z_t > z_b \text{ set } z_b = z_t \\ \text{if } z_d < z_b \text{ set } z_b = z_d \,. \end{array} \tag{18}$$

[16] The composite hydrate inventory (sum over seafloor depth levels $i = 1, \ldots, n$) then is

$$M_H = \sum_i m_H^i = \sum_i a_H^i \, c_H^i \, \{z_b - z_t\}_{z_0^i} \,. \tag{19}$$
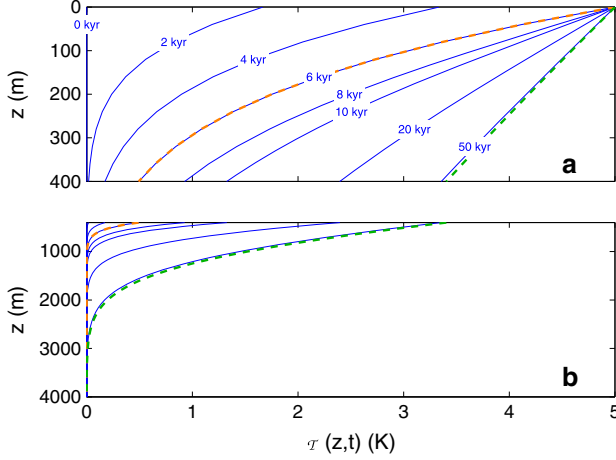
Figure 3. Calculated temperature anomaly profiles at various times (labels in kyr) after onset ($t = 0$) of temperature perturbation at SWI. Panels show the same curves: (a) 0–400 m, (b) 400–4000 m. Latent heat from hydrate dissociation is not considered. The end of the initial warming phase is $t_w = 6$ kyr, the main phase duration is $t_m = 50$ kyr. (see Figure 1). Analytical solution for $0 \leq t \leq t_w$ (equation (25)) at $t = t_w = 6$ kyr (orange dashed line) and analytical solution for $t \gg t_w$ (equation (26)) at $t = t_m = 50$ kyr (see text) (green dashed line).

Individual areas, a_H^i, and hydrate concentrations, c_H^i, are not well known and will be assumed constant in a first step. In that case, it follows $A_H = n\, a_H^i$, where A_H is the global hydrate area, and

$$M_H = \frac{A_H c_H}{n} \sum_i \{z_b - z_t\}_{z_0^i} . \tag{20}$$

Below, we are mainly interested in the relative inventories and fluxes from different depths over time, rather than absolute values. Thus, we may simply measure the hydrate inventory at a given seafloor depth z_0 in units of length (ignoring area and concentration):

$$l_H(z_0) = \{z_b - z_t\}_{z_0} \quad \begin{array}{l} \text{if } z_t > z_b \text{ set } z_b = z_t \\ \text{if } z_d < z_b \text{ set } z_b = z_d . \end{array} \tag{21}$$

The composite hydrate inventory normalized to n (i.e., invariant to the choice of n) is

$$L_H = n^{-1} \sum_i l_H^i = n^{-1} \sum_i \{z_b - z_t\}_{z_0^i} , \tag{22}$$

so that $A_H\, c_H\, L_H$ yields the global hydrate inventory. The dissociation "flux" at each seafloor depth level z_0^i in m y^{-1} is

$$F_i^* = -\frac{d l_H^i}{dt} , \tag{23}$$

where the asterisk indicates that F_i^* needs to be multiplied by area and concentration to obtain a mass flux. Finally, the n-normalized composite dissociation flux is

$$F^* = n^{-1} \sum_i F_i^* . \tag{24}$$

3. Analytical and Numerical Solution

3.1. Linear Temperature Forcing Over Time

[17] For a linear temperature increase over time at the upper model boundary (SWI), i.e., $T(z = 0, t) = a \times t$, equation (4) can be solved analytically with solution [*Carslaw and Jaeger*, 1959]

$$\mathcal{T}(z, t) = 4\, a\, t\, i^2 \text{erfc}\left(\frac{z}{2\sqrt{\kappa t}}\right) \tag{25}$$

where a is the initial warming rate at $z = 0$ (in K kyr^{-1}) and the function $i^2\text{erfc}(x)$ is given in Appendix B. This analytical solution is valid during the time interval of the initial bottom water warming ($0 \leq t \leq t_w$, see Figure 1) and provides a useful check for the numerical solution (Figure 3).

3.2. Initial Temperature Jump

[18] For $t \gg t_w$ and $t \leq t_m$ (t_m being the main phase duration, see Figure 1), the profile approaches the solution for an initial temperature jump because the memory of the initial temperature rise has been lost. Hence, the solution for an instantaneous initial warm-up should provide a good approximation [*Carslaw and Jaeger*, 1959]:

$$\mathcal{T}(z, t) = \mathcal{T}(0, t_w)\, \text{erfc}\left(\frac{z}{2\sqrt{\kappa t}}\right) , \tag{26}$$

where the complementary error function is given in Appendix B. This analytical solution may be compared to the numerical solution, for instance, at $t = t_m$ (Figure 3).

3.3. Numerical Solution

[19] The full problem was solved numerically using a Crank-Nicolson scheme [*Crank and Nicolson*, 1947; *Press et al.*, 1992], with and without latent heat uptake from hydrate dissociation (equations (4) and (15)). The boundary conditions were set as described in section 2.3, with a
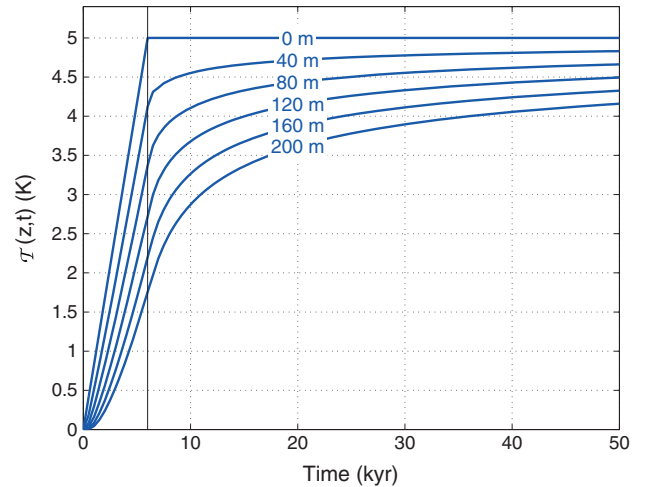

Figure 4. Simulated evolution of temperature anomaly at different sediment depths (labels in m) as a function of time. Latent heat from hydrate dissociation is not considered. The subsurface sediments e.g., at $z = 200$ m keep warming by >2 K for 50 kyr after the temperature at the sediment-water interface at $z = 0$ m remains constant (after $t = 6$ kyr, black vertical line).
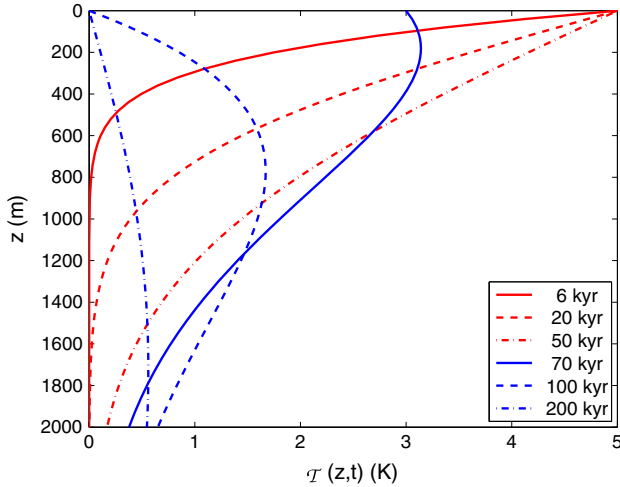
5

Figure 5. Calculated temperature profiles in the sediment at various times between 6 and 200 kyr in response to the temperature forcing at the SWI are shown in Figure 1. Latent heat from hydrate dissociation is not considered. Note that sediments at $z > 600$ m keep warming between 50 and 70 kyr, although the SWI is already cooling.

lower flux boundary condition (geothermal heat flux) at a typically large $h = 4$ km to avoid any damping of the temperature anomaly (section 2.3). When latent heat uptake was ignored, the numerical algorithm was stable and accurate, for instance, at a typical time step and grid spacing of $\Delta t = 500$ y and $\Delta z = 40$ m (accuracy checked by comparing to analytical solution). Note that while the Crank-Nicolson scheme for diffusion is unconditionally stable, errors are minimized for small $\kappa \Delta t/(\Delta z)^2$. When latent heat uptake was included, the grid spacing and the time step were reduced to avoid numerical instabilities ($\Delta t = 10$ y, $\Delta z = 1$ m). In addition, the latent heat uptake at a single grid point was distributed over several grid points and time steps.

4. Results I: Without Latent Heat Uptake

[20] The analytical and numerical results confirm that a temperature anomaly generated at the SWI requires several thousand years to reach a sediment depth of a few hundred meters (latent heat uptake from hydrate dissociation will not change this result, see below). For example, for a bottom water warming of 5 K over 6 kyr, sediments at $z = 200$ m show only about half the warming after 8 kyr (Figure 3). This is consistent with the simple estimate of the characteristic time scale of heat transfer in sediments (section 2.1). Subsurface sediments e.g., at $z = 200$ m keep warming by >2 K over 50 kyr after the temperature at the sediment-water interface at $z = 0$ m remains constant (after $t = 6$ kyr, see Figure 4). The slow subsurface warming has consequences for the timing of potential methane hydrate dissociation. For instance, all hydrates within a specific zone (between 6 and 50 kyr profiles in Figure 3) and within the initial hydrate stability zone would slowly dissociate over tens of thousands of years (see below). Note that even though the SWI starts cooling after 50 kyr, sediments at $z > 600$ m keep warming for several tens of thousands of years after that (Figure 5). However, this has little consequences for potential hydrate

dissociation because methane hydrates are generally unstable at this sediment depth and therefore do not exist there (see Figure 2).

5. Results II: With Latent Heat Uptake

5.1. Temperature Profiles

[21] The numerical results show that the latent heat uptake from hydrate dissociation delays subsurface warming at a few hundred meter below seafloor by ~1 kyr after ~6 kyr (Figure 6). However, the difference between runs with and without latent heat uptake progressively decreases as time proceeds. Thus, on time scales of tens of thousands of years, the effect of hydrate dissociation on the modeled heat transfer in sediments becomes less important. It follows that the main results presented above without considering latent heat uptake from hydrate dissociation remain unchanged.

5.2. Hydrate Dissociation Flux

[22] Given a methane hydrate stability zone and potential deposition zone (Figure 2), and the simulated evolution of the temperature anomaly that triggers hydrate dissociation in the sediment (Figure 6), a dissociation flux can be calculated over time based on equations (23) and (24). For simplicity, the calculations assume a potential hydrate deposition zone of 150 m thickness extending from $z_t = 20$ mbsf to $z_d = 170$ mbsf. Note, however, that the actual hydrate layer is much thinner at shallow water depth because of a shallow stability base in the sediment (Figure 2). Methane hydrate reservoirs (three such reservoirs are shown in Figure 2) were distributed evenly over the depth range between 1000 and 3200 m below sea level, and two different configurations were tested: discrete reservoirs separated by depth intervals of 100 and 10 m, respectively. In other words, individual fluxes were calculated for 23 and 221 discrete reservoirs at different depth levels z_0, respectively, from which composite fluxes were determined for each of the two configurations. Regardless of the depth intervals, the results show that a substantial fraction of the hydrate dissociation only occurs after the initial warming phase is complete ($t > t_w$, see Figure 7). For instance, sediments at >1600 m water depth show a long tail of methane release beyond t_w, while sediments at >2500 m water depth only start releasing methane after t_w (Figure 7).

[23] The prolonged release is a direct consequence of the slow propagation of the temperature anomaly generated at
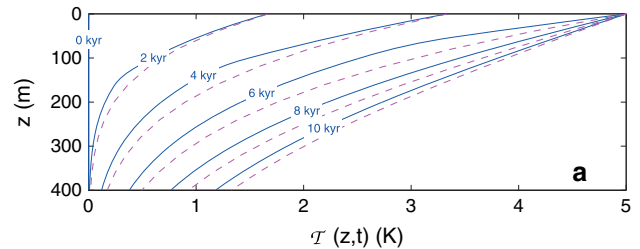

Figure 6. Temperature anomaly profiles at various times (labels in kyr) after onset ($t = 0$) of temperature perturbation at SWI with (solid blue lines) and without (dashed magenta lines) latent heat from hydrate dissociation (compare Figure 3).
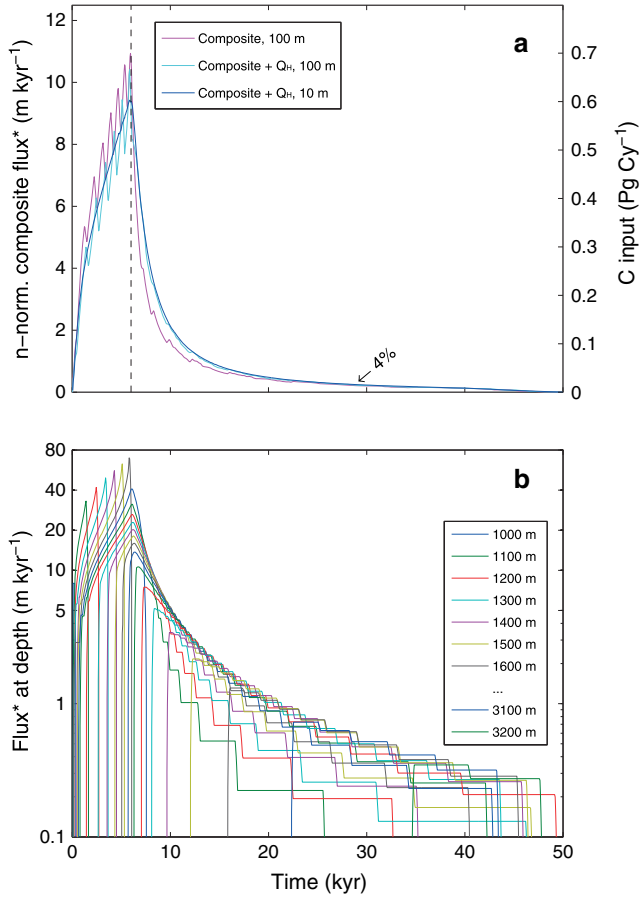
Figure 7. Calculated methane hydrate dissociation fluxes. Asterisks indicate that quantities need to be multiplied by area and concentration to obtain a mass flux (see text). (a) Normalized, composite fluxes (equation (24)). Carbon input rate (right axis) shown for 4500 Pg C total input over 50 kyr (initial pulse + bleeding) [*Zeebe et al.*, 2009]. The sum of the fluxes shown in Figure 7b divided by the total number of depth levels (n) yields the corresponding n-normalized composite flux (cyan line). Composite flux without considering latent heat uptake, depth level increments of 100 m (magenta line). Composite flux including latent heat uptake, depth level increments of 10 m (fluxes at depth not shown) (blue line). The vertical dashed line indicates the end of the initial warming phase (t_w). After ∼30 kyr (arrow), the composite flux drops to 4% of the average composite flux during the first 6 kyr. (b) Individual fluxes from various water depths (equation (23)). Note the logarithmic vertical axis. Graphs show dissociation fluxes from discrete hydrate reservoirs separated by depth intervals of 100 m throughout the range from 1000 to 3200 m depth below sea level (a periodic sequence of seven colors is used to represent all depth levels). Calculations include latent heat uptake from hydrate dissociation (Q_H).

the seafloor into deeper sediment sections (Figure 4). Note that hydrate dissociation usually starts at the base of the hydrate layer, particularly at greater water depth. For example, at 2200 mbsl and an initial bottom water temperature of 11°C, the temperature at the top of the hydrate layer may still be below the critical dissociation temperature even after the SWI has warmed by 5 K (Figure 2c). In contrast, at the same time, the base of the stability zone (intersection of geotherm and stability curve) has moved upward, causing hydrate dissociation at the base of the hydrate layer. Because the temperature anomaly generated at the SWI requires several thousand years to reach a few hundred meter sediment depth—and hence to reach the base of the hydrate layer—there is a substantial delay between bottom water warming and the onset of the hydrate dissociation flux at greater water depth (Figure 7). In addition, at greater water depths, the hydrate stability zone is thicker than at shallow water depth (Figures 2a and 2c). This causes slow and prolonged hydrate dissociation at greater water depth as the dissociation front slowly rises upward through the hydrate layer. In contrast, complete and more rapid hydrate dissociation may occur at shallow water depth, where the stability base is located closer to the ocean floor and warms up quicker.

[24] The release dynamics at different water depths have important consequences for the evolution of the composite dissociation flux over time (Figure 7). First, if the bottom water warming occurs over several thousand years, the onset of the dissociation flux (i.e., carbon input into the exogenic reservoir) is not abrupt but increases more gradually, particularly toward the end of the initial warming phase. Second, the dissociation flux has a long tail. In other words, the carbon release continues for more than 30 kyr after the onset of the initial warming (Figure 7). Applying this result to the PETM, how does the relative magnitude of the carbon fluxes over time compare to previous simulations that included prolonged carbon input? For example, in order to match PETM observations, *Zeebe et al.* [2009] used an initial carbon pulse of 0.5 Pg C y^{-1} (3000 Pg C over 6 kyr) and a subsequent carbon bleeding of ∼0.02 Pg C y^{-1} (1500 Pg C over 70 kyr). In other words, the bleeding rate amounted to 4% of the initial rate. For comparison, relative to the average composite dissociation flux during the first 6 kyr as calculated here, the composite flux drops to 4% after ∼30 kyr (Figure 7). Thus, the relative magnitude of initial pulse versus bleeding fluxes from methane hydrate dissociation over this time interval is consistent with constraints from global carbon cycle modeling. However, note that the present calculations do not support significant carbon input from hydrate dissociation much beyond ∼40 kyr.

6. Discussion

[25] The results of the calculations presented above show that slow methane hydrate dissociation would have caused a small but continued carbon release that extended substantially beyond ∼10 kyr of the initial PETM warming (Figure 7). I suggest that this slow methane release contributed to the long duration of the PETM. In this context, it is important to reiterate that a first pulse, as well as a continued carbon release from methane hydrate dissociation during the PETM, would have acted as a feedback to some initial warming rather than the trigger of the event. In addition

to slow methane release from oceanic hydrates, other feed-backs may have contributed to a prolonged carbon input and warming during the PETM. Several of these feedbacks will be discussed below (sections 6.2–6.7).

6.1. Previous Studies

[26] The results for the methane hydrate dissociation flux obtained here (Figure 7) may be compared to the results of *Xu et al.* [2001], who modeled the methane flux from a gas hydrate layer in response to a 4 K warming under modern and late Paleocene conditions. However, there are several important differences between the two studies. First, *Xu et al.* [2001] only considered a single hydrate layer at 1200 m water depth, whereas a series of layers between 1000 and 3200 m water depth is considered here. Second, *Xu et al.* [2001] used a half-sine temperature perturbation with a maximum of 4 K, which lasted for 10 kyr and was zero thereafter, whereas a 5 K temperature perturbation was used here that lasted for 50 kyr (Figure 1). Despite the differences, it is interesting to note that Xu et al.'s calcu-lated methane flux across the seafloor from a single hydrate layer for late Paleocene conditions remained elevated above its initial value even after 50 kyr. The propagation of the temperature anomaly as calculated here (Figure 3) may be compared to the results of *Katz et al.* [2001]. However, *Katz et al.* [2001] only focused on the first 10 kyr following the onset of the PETM and assumed an instantaneous bottom water temperature increase of 5 K, which, as the authors pointed out as well, is unrealistically fast. Neither *Xu et al.* [2001] nor *Katz et al.* [2001] included latent heat uptake from hydrate dissociation in their analyses.

[27] As mentioned above, stable carbon and oxygen iso-tope records, Mg/Ca ratios, and B/Ca ratios indicate pro-longed changes in surface ocean temperature and carbonate chemistry during the PETM for at least 50 kyr [*Röhl et al.*, 2007; *Farley and Eltgroth*, 2003; *Murphy et al.*, 2010; *Charles et al.*, 2011; *Penman et al.*, 2011; *Zeebe and Zachos*, 2013]. Numerous of these records require prolonged carbon bleeding in models to match the observations [e.g., *Zeebe et al.*, 2009; *Penman et al.*, 2011; *Zeebe and Zachos*, 2013]. However, note that *Cui et al.* [2011] suggested excess car-bon drawdown after ~20 kyr in a model scenario with a very large initial carbon input to match an organic carbon isotope record from Spitsbergen. This could indicate that the inferred carbon bleeding/uptake is sensitive to uncertainties in the data, stratigraphy, and model parameters. It could also indicate a particular feature of the Spitsbergen record when combined with a very large initial carbon input in the model [*Sluijs et al.*, 2012; *Cui et al.*, 2012].

6.2. Lack of Hydrate Deposition During the PETM

[28] A bottom water warming of 5 K during the PETM would not only have caused widespread dissociation of methane hydrates in the deep sea but also prevented deposi-tion of new hydrates for tens of thousands of years across a large seafloor area. Even after bottom waters started cooling, temperatures in the sediment column would have remained elevated over time scales of 10^4 y (Figure 5). Hence, the hydrate deposition flux (a methane sink) was strongly reduced during the warmth of the PETM relative to the steady state deposition flux before the PETM. On a net basis, this represents an additional carbon source to the exogenic

reservoir in the form of methane, which, under most circum-stances, is quickly oxidized to CO_2 [*Schmidt and Shindell*, 2003; *Kessler et al.*, 2011; *Joye et al.*, 2011; *Carozza et al.*, 2011]. The relationship between bottom water tempera-ture and methane hydrate deposition in sediments constitutes a positive feedback, which releases additional carbon dur-ing warming and enhances carbon storage during cooling. Possible cooling triggers include weathering of carbonate and silicate rocks (ultimately reducing atmospheric CO_2 concentrations) and the cessation of the methane hydrate dissociation flux (Figure 7).

[29] The magnitude of the steady state hydrate production (recharge) flux is uncertain. Within the sediment, methane can cycle between dissolved gas, free gas, and gas hydrate. For the steady state flux from free gas to hydrate, *Dickens* [2003] assumed a flux on the order of 0.001 Pg C y^{-1}. A rough estimate may be obtained by considering the recharge time between Paleogene hyperthermals. For example, the Elmo event occurred about 2 myr after the PETM [*Lourens et al.*, 2005]. Assuming a total carbon release (pulse + bleed-ing) of 4500 Pg C during the PETM from methane hydrates [*Zeebe et al.*, 2009] and half the PETM's carbon release dur-ing Elmo, methane hydrates would have accumulated at least 4500/2 = 2250 Pg C over 2 my, giving a recharge flux of 0.0011 PgCy^{-1}. If these estimates are correct, then the addi-tional carbon input due to a lack of hydrate deposition during the PETM would have contributed only about 5% of the total bleeding flux of 0.02 PgCy^{-1} postulated by *Zeebe et al.* [2009].

6.3. Additional Carbon Release From Marine Sediments

[30] It is well known that metabolic rates of microbially-mediated processes are sensitive to temperature. For exam-ple, the so-called Q_{10}-rule states that metabolic rates roughly double for every 10 K increase in temperature ($Q_{10} = 2$). Thus, for a 5 K temperature increase during the PETM, metabolic rates would have increased by about 40%, includ-ing aerobic breakdown rates of organic carbon, sulfate reduction (SR), methanogenesis (MG), and anaerobic oxi-dation of methane (AOM) in marine sediments. The critical point with respect to the PETM carbon bleeding is that such increased rates would not only have to promote more rapid carbon turnover but need to mobilize previously stored car-bon. In marine sediments, this includes processes such as SR and AOM, whose ultimate carbon source is sedimentary organic matter. Modern estimates of total marine SR and AOM fluxes vary from 8 to 66×10^{12} mol S y^{-1} and from 4 to 24×10^{12} mol C y^{-1} (0.05 to 0.3 Pg C y^{-1}), respectively [e.g., *Turchyn and Schrag*, 2006; *Canfield et al.*, 2005; *Reeburgh et al.*, 1993; *Hinrichs and Boetius*, 2002; *Valentine*, 2002; *Catling et al.*, 2007]. Despite the uncertainties, these num-bers suggest that both processes are quantitatively important. Aerobic oxidation of organic carbon in marine sediments is undoubtedly an important process as well. However, it is unclear whether this process increased during the PETM because seawater oxygen concentrations were most likely reduced [e.g., *Dickens*, 2000; *Chun et al.*, 2010; *Dickson et al.*, 2012]. The following discussion starts with the anaero-bic oxidation of methane because methane has been the main focus of this paper so far.
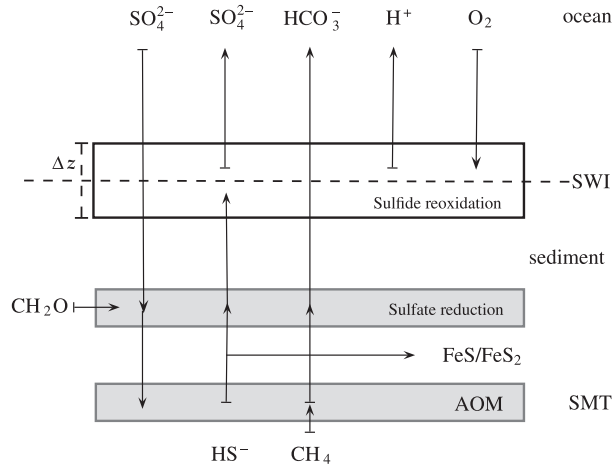
Figure 8. Schematic illustration of fluxes during sulfate reduction (SR) and anaerobic oxidation of methane (AOM). SWI = Sediment-water interface; SMT = sulfate-methane transition. Note that SR and AOM can occur independently, depending on location. If they occur together, their zones do not necessarily have to be spatially separated. While fluxes within the sediment in a finite porewater volume at the site of SR and AOM may follow a simple stoichiometry according to the net chemical reactions (see text), this is not the case for the fluxes across the SWI. A large fraction of the sulfide is reoxidized to sulfate at or near the SWI. Consider a box with vertical dimension Δz enclosing the SWI and covering the SR and/or AOM seafloor area. The net flux balance for the ocean is represented by the sum of the fluxes across the top of the box.
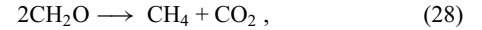
6.4. Anaerobic Oxidation of Methane (AOM)

[31] The net reaction for the anaerobic oxidation of methane may be written as

$$CH_4 + SO_4^{2-} \xrightarrow{k_{AOM}} HCO_3^- + HS^- + H_2O, \qquad (27)$$
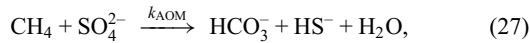
where k_{AOM} is a temperature-dependent, microbially-mediated rate constant. Reaction (27) suggests that at higher metabolic rates due to elevated temperatures, additional carbon could be released from sediments in the form of HCO_3^-. Considering the bottom water warming and sediment warming during the PETM as calculated above, the additional HCO_3^- release from AOM might therefore have contributed to the long-term carbon release and hence to the long-term warming during the event. However, there are at least two issues that complicate this simple view. First, reaction (27) also leads to changes in total alkalinity (TA) as SO_4^{2-} is consumed and HCO_3^- is produced (for a detailed discussion of TA, see *Zeebe and Wolf-Gladrow* [2001] and *Wolf-Gladrow et al.* [2007]). Possible changes in the alkalinity flux from sediments to the ocean are critical because they would affect whole-ocean carbonate chemistry, carbonate sediment dissolution, and the atmospheric CO_2 concentration. Second, the Q_{10}-rule not only applies to AOM but to various metabolic processes, including sulfate reduction and methanogenesis (MG). For example, MG produces isotopically light CH_4

(depleted in ^{13}C) but also isotopically heavy CO_2 (enriched in ^{13}C), with a net reaction:

$$2CH_2O \longrightarrow CH_4 + CO_2, \qquad (28)$$

where CH_2O represents organic matter. The heavy CO_2 released during the process could affect the overall carbon isotope composition of the released carbon (see below).

6.4.1. Alkalinity Fluxes During Anaerobic Oxidation of Methane

[32] According to reaction (27), total alkalinity (TA) and total dissolved inorganic carbon (DIC) in porewater increase in a molar ratio of 2:1 for each mole of CH_4 and SO_4^{2-} consumed during AOM [*Zeebe and Wolf-Gladrow*, 2001; *Wolf-Gladrow et al.*, 2007; *Zeebe*, 2007]. However, this TA:DIC ratio applies to the fluxes within a finite porewater volume at the site of AOM in the sediment (usually at the sulfate-methane transition, SMT), but not to the net flux ratio across the SWI. Due to sulfide oxidation at or near the SWI

$$HS^- + 2\,O_2 \longrightarrow SO_4^{2-} + H^+, \qquad (29)$$
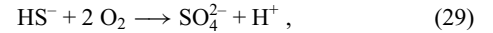
often only a small fraction of the alkalinity carried upward through the sediment column by HS^- is actually released to the ocean (Figure 8). Instead, in the case of reoxidation, SO_4^{2-} and H^+ are returned to the ocean [*Jørgensen and Kasten*, 2006]. Thus, combining reactions (27) and (29), for each mole of SO_4^{2-} taken up from seawater during AOM, one mole of SO_4^{2-}, HCO_3^-, and H^+ (equivalent to $CO_2 + H_2O$) may be returned to the ocean. Note that uptake and release of SO_4^{2-} from/to seawater reduces and raises the ocean's alkalinity by two units, respectively. As a result, in the case of complete sulfide reoxidation, the net TA balance for the ocean from AOM is zero. In fact, observations indicate that in coastal marine sediments, some 90% of all the sulfide produced is lost by reoxidation at the sediment surface [e.g., *Jørgensen*, 1977; *Jørgensen and Kasten*, 2006]. It has therefore been argued that alkalinity fluxes from HS^- may be ignored in benthic TA budgets in coastal and shelf environments [*Krumins et al.*, 2013].

[33] However, this assumption breaks down in sediment settings where a significant fraction of HS^- is precipitated as iron sulfide and pyrite in sediments [e.g., *Berner*, 1982] (see Figure 8). For example, in the modern ocean, iron sulfide/pyrite formation in sediments occurs in various locations including the Black Sea and continental margins such as the Argentine Basin [*Jørgensen et al.*, 2004; *Hensen et al.*, 2003], which may be represented by

$$HS^- + Fe^{2+} \longrightarrow FeS + H^+. \qquad (30)$$
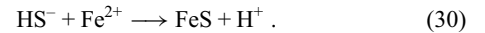
Reaction (30) implies a reduction of TA in porewater by two moles per mole of HS^- consumed. Note that iron is usually mobilized and reprecipitated within the sediment and may be ignored for the ocean's alkalinity balance. Thus, combining reactions (27) and (30), for each mole of SO_4^{2-} taken up from seawater during AOM, one mole of HCO_3^- and H^+ (equivalent to $CO_2 + H_2O$) may be returned to the ocean. As a result, in the case of complete precipitation of total sulfide ($TH_2S = [H_2S] + [HS^-]$) as FeS, the net flux balance ratio of TA:DIC for the ocean is 2:1.

[34] In extreme settings such as the Black Sea with massive concentrations of reactive iron and FeS/FeS$_2$ formation,

the upward TH_2S flux toward the sediment surface may vary between 7% and 21% of the SO_4^{2-} consumed during AOM [*Jørgensen et al.*, 2004]. Furthermore, *Jørgensen et al.* [2004] estimated that 57–73% may be trapped within the CH_4 oxidation zone, due to reaction with iron and reoxidation of the sulfide. If half of the trapped TH_2S is reoxidized, then the trapped and upward flux due to reoxidation amounts to 36–58% of the AOM uptake of SO_4^{2-}. These numbers probably represent an end-member scenario in environments with exceptionally large iron sulfide formation and low reoxidation of TH_2S. The other end-member scenario may be represented by coastal marine sediments, with 90% reoxidation at the sediment surface (see above). Thus, a tentative global average of TH_2S reoxidation may be taken as 80% of the consumed SO_4^{2-}, consistent with previous estimates ranging from 80% to >98% [e.g., *Turchyn and Schrag*, 2006; *Jørgensen and Kasten*, 2006]. In summary, the overall net flux balance ratio of TA:DIC during AOM for the ocean is probably closer to 0.4:1, where the relative change in TA is estimated by weighing the end-member scenarios discussed above ($0 \cdot 0.8 + 2 \cdot 0.2 = 0.4$).

[35] Note that a smaller fraction of the HCO_3^- produced during AOM may precipitate as $CaCO_3$ in the sediment:

$$Ca^{2+} + HCO_3^- \longrightarrow CaCO_3 + H^+ , \qquad (31)$$

which tends to reduce ocean TA as Ca^{2+} is taken up from seawater. Carbonate precipitation during AOM also reduces the efflux of HCO_3^- from sediments and hence the DIC input to the ocean.

[36] Finally, assuming that AOM increased during the PETM, causing continuous carbon release over time scales >10 kyr, what would have been the effect of the additional alkalinity release on ocean chemistry and atmospheric CO_2? For example, including a long-term TA release (molar TA:C input ratio = 0.4:1) in the standard PETM simulation of *Zeebe et al.* [2009] reduces atmospheric CO_2 during the main phase by $\sim$40 ppmv. This is a small effect relative to a total CO_2 concentration of $\sim$1700 ppmv, partly due to the fact that ocean TA is already high during the main phase from $CaCO_3$ dissolution and enhanced weathering [*Zeebe*, 2012].

6.5. Sulfate Reduction (SR)

[37] Analogous to AOM, dissimilatory sulfate reduction, represented by

$$2\,CH_2O + SO_4^{2-} \longrightarrow 2\,HCO_3^- + H_2S \qquad (32)$$

may also have increased during the PETM as a result of bottom water warming and sediment warming. Furthermore, regarding carbon release and HS^- reoxidation, similar arguments can be made for SR as for AOM (Figure 8). However, the TA:DIC ratio implied by reaction (32) is 1:1 for each mole of SO_4^{2-} consumed. Also, the carbon isotope composition of the HCO_3^- released should be close to that of organic carbon (represented by CH_2O), rather than methane (see below). Assuming again that 80% of HS^- is reoxidized, the overall net flux balance ratio of TA:DIC during SR for the ocean is 0.2:1 (in this case, weighing the end-member scenarios gives a relative change in TA of $0.2 = 0 \cdot 0.8 + 1 \cdot 0.2$). Thus, the effect of alkalinity release on pCO_2 during the

PETM due to enhanced sulfate reduction would be even smaller than for AOM per mole of carbon released.

6.6. Stable Carbon Isotope Ratios

[38] One of the prominent features of the PETM is a sustained, negative global carbon isotope excursion (CIE) of about 3‰ that lasted as long as the warming (the warming has been inferred from other independent proxies including oxygen isotopes and Mg/Ca ratios). To match the observed CIE duration in a global carbon cycle model, *Zeebe et al.* [2009] assumed a carbon bleeding with a source $\delta^{13}C$ of –50‰. This value points to a strongly ^{13}C-depleted carbon source such as methane. What are the carbon isotope compositions of the potential long-term carbon sources discussed above?

[39] Prolonged methane hydrate dissociation due to slow heat transfer in marine sediments (section 5.2), lack of hydrate deposition during the PETM (section 6.2), and anaerobic oxidation of methane (section 6.4) all release methane, which is strongly depleted in ^{13}C. As mentioned above, methanogenesis (MG) produces isotopically light CH_4 (depleted in ^{13}C) but also isotopically heavy CO_2 (enriched in ^{13}C). However, the effect of ^{13}C-enriched CO_2 on the $\delta^{13}C$ profile of porewater DIC is often only visible deep in the sediment column and substantially below the sulfate-methane transition (SMT), the latter of which is dominated by AOM and input of isotopically light carbon [e.g., *Paull et al.*, 2000; *Malinverno and Pohlman*, 2011]. On time scales of 10^4 y, it is therefore more likely that the $\delta^{13}C$ of the carbon flux across the SWI is dominated by light carbon from enhanced AOM, rather than heavy carbon from enhanced MG from below the SMT. This is because the time scale of diffusion in the sediment column scales with the square of the sediment depth—just as heat transfer, see equation (5). In other words, it takes significantly longer for carbon from a deep sediment source to cross the SWI than from a shallow source. The carbon isotope composition of HCO_3^- produced during sulfate reduction (section 6.5) should be very close to that of organic carbon, i.e., around –25‰.

[40] In summary, with the exception of sulfate reduction, all potential carbon bleeding sources discussed above likely release carbon that is strongly depleted in ^{13}C. For example, the $\delta^{13}C$ of biogenic methane typically ranges from –90‰ to –55‰. If a combination of enhanced methane sources and SR ($\delta^{13}C \simeq$ –25‰) were active during the PETM main phase, an overall carbon isotope composition of –50‰ for the bleeding source as assumed by *Zeebe et al.* [2009] appears plausible.

6.7. Water Column Remineralization

[41] In addition to effects of temperature on metabolic processes in sediments, ocean warming would also affect metabolic processes in the water column such as remineralization of organic carbon exported from the surface layer. However, it is emphasized that enhanced recycling of carbon in the water column does not mobilize additional carbon that could contribute to explaining the carbon bleeding during the main phase of the PETM. Nevertheless, changes in water column remineralization affect the concentration of CO_2 in the atmosphere; hence, this process is included in the discussion here for completeness.

[42] For example, under preindustrial conditions, *Matsumoto* [2007] found a 35 ppmv increase in atmospheric CO_2 after 1 kyr in the intermediate complexity model GENIE-1 due to enhanced remineralization in response to a 5 K ocean warming. For comparison, the Long-term Ocean-atmosphere-Sediment CArbon cycle Reservoir (LOSCAR) model [*Zeebe*, 2012] gives +45 ppmv after 20 kyr in a corresponding preindustrial setup. For a 5 K warming, the percentage of carbon remineralized between the mixed layer (export = 100%) and 1000 m water depth was globally increased from 78% to 88% in LOSCAR, corresponding to a global mean increase from 81% to 91% in GENIE-1 (K. Matsumoto, personal communication, 2013). The stronger response in the box model is probably due to a higher sensitivity of box model pCO_2 to changes in ocean biogeochemistry. Using LOSCAR and applying the same change in remineralization (78% to 88%) to the standard PETM simulation of *Zeebe et al.* [2009] raises atmospheric CO_2 by ∼200 ppmv during the main phase. This value probably represents an upper limit because the effect is likely smaller in intermediate complexity models and even smaller in general circulation models [*Kwon et al.*, 2009]. Nevertheless, a CO_2 increase of this magnitude would be significant as it might help solve the PETM climate sensitivity conundrum [*Zeebe et al.*, 2009]. The calculated atmospheric CO_2 increase during the PETM based on the carbon input alone appears insufficient to explain the full magnitude of the inferred warming when standard values for the climate sensitivity are assumed [*Zeebe et al.*, 2009]. Hence, additional processes augmenting the pCO_2 rise such as changes in remineralization would help reconcile temperature and pCO_2 estimates, without having to invoke excessively large values for the climate sensitivity.

6.8. Limitations and Issues

[43] The results of the present study should be considered in light of several limitations. For example, the hydrate dissociation flux calculated above is based on a simple model of hydrate depth distribution and hydrate concentration in the sediment pore space. Unfortunately, these quantities are poorly known and enhanced observational efforts would help to better constrain these parameters. Likewise, as mentioned above, there are large uncertainties associated with modern estimates of global metabolic rates of sedimentary organic carbon remineralization. Improving such estimates is an obvious challenge for the present and even more so for the past. In terms of the modeling, further numerical simulations appear desirable that include a full interactive feedback between methane release from marine gas hydrate systems, increases in atmospheric greenhouse gas concentrations, surface warming and deep ocean warming, and further methane release. However, simulations of this type are not a small task because they require a coupled climate-carbon cycle model that also includes heat transport in sediments and calculates fluxes of methane to/from marine gas hydrate systems. Such a fully coupled model could ultimately be forced with observed records to yield carbon input rates over time [cf. *Cui et al.*, 2011]. Finally, it should be realized that the present study entirely focuses on marine processes as possible causes for a sustained carbon release during the PETM. Future work should also consider terrestrial processes.

7. Conclusions

[44] Identifying the cause for the long duration of the PETM is important both for our fundamental understanding of carbon cycle-climate feedbacks and for long-term projections of future warming from anthropogenic greenhouse gas emissions. In this study, I have presented an analysis of heat conduction in marine sediments, showing that after bottom waters warmed during the PETM, it took tens of thousands of years for a temperature anomaly to diffuse to a sediment depth of a few hundred meters. This would have caused slow methane release from marine gas hydrate systems substantially beyond the time interval of the initial warming (>10 kyr). I suggest that the slow methane release contributed to a sustained carbon release and hence the long duration of the PETM. Additional carbon may have been released through processes such as temperature-enhanced mineralization of sedimentary organic carbon and the absence of methane hydrate deposition during the PETM.

[45] In terms of relevance to future warming, methane release from marine gas hydrate systems could play an important role as a slow long-term carbon and warming source in the future [e.g., *Archer et al.*, 2009]. However, because of differences in initial conditions, marine hydrate dissociation is likely to have a smaller impact during comparatively "cold" periods such as the preindustrial era than during warm periods such as the Paleocene/Eocene [*Xu et al.*, 2001]. Finally, additional long-term carbon release from temperature-enhanced mineralization of sedimentary organic carbon is equally possible for the future as for the PETM.

Appendix A: Solution of Steady State Advection-Diffusion Equation

[46] The general solution to equation (7) may be written as ($\lambda = w/\kappa$)

$$T = A\,e^{\lambda z} + B\,. \tag{A1}$$

Using boundary conditions $T(0) = T_0$, $T(h) = T_0 + G_0h$, with h being the base of the geotherm, leads to

$$T_0 = A + B \tag{A2}$$

$$T_0 + G_0h = A\,e^{\lambda h} + B\,, \tag{A3}$$

which can be solved for A and B

$$A = G_0h(e^{\lambda h} - 1)^{-1}; \quad B = T_0 - A\,. \tag{A4}$$

Inserting into equation (A1) gives

$$T = A\,e^{\lambda z} + T_0 - A = A(e^{\lambda z} - 1) + T_0 \tag{A5}$$

and hence the solution

$$T = T_0 + G_0h(e^{wz/\kappa} - 1)/(e^{wh/\kappa} - 1)\,. \tag{A6}$$

Appendix B: Error Functions

[47] The function $i^2\mathrm{erfc}(x)$ is given by

$$i^2\mathrm{erfc}(x) = \frac{1}{4}\left[(1 + 2x^2)\mathrm{erfc}(x) - \frac{2}{\sqrt{\pi}}\,x\,e^{-x^2}\right]\,, \tag{B1}$$

with complementary error function

$$\mathrm{erfc}(x) = \frac{2}{\sqrt{\pi}}\int_x^\infty e^{-s^2}\mathrm{d}s\,. \tag{B2}$$

References

Adkins, J. F., and D. P. Schrag (2003), Reconstructing Last Glacial Maximum bottom water salinities from deep-sea sediment pore fluid profiles, *Earth Planet. Sci. Lett.*, *216*, 109–123, doi:10.1016/S0012-821X(03)00502-8.

Archer, D., B. Buffett, and V. Brovkin (2009), Ocean methane hydrates as a slow tipping point in the global carbon cycle, *Proc. Nat. Acad. Sci.*, *106*(49), 20,596–20,601, doi:10.1073/pnas.0800885105.

Berner, R. A. (1982), Burial of organic carbon and pyrite sulfur in the modern ocean; its geochemical and environmental significance, *Am. J. Sci.*, *282*(4), 451–473, doi:10.2475/ajs.282.4.451.

Bice, K. L., and J. Marotzke (2002), Could changing ocean circulation have destabilized methane hydrate at the Paleocene/Eocene boundary? *Paleoceanography*, *17*(2), 1018, doi:10.1029/2001PA000678.

Brown, K. M., N. L. Bangs, P. N. Froelich, and K. A. Kvenvolden (1996), The nature, distribution, and origin of gas hydrate in the Chile Triple Junction region, *Earth Planet. Sci. Lett.*, *139*, 471–483, doi:10.1016/0012-821X(95)00243-6.

Canfield, D. E., B. Thamdrup, and E. Kristensen (2005), *Aquatic Geomicrobiology, Advances in Marine Biology*, 640 pp., vol. 48, Elsevier Academic Press, Amsterdam.

Carlson, R. L., and C. N. Herrick (1990), Densities and porosities in the oceanic crust and their variations with depth and age, *J. Geophys. Res.*, *95*(B6), 9153–9170, doi:10.1029/JB095iB06p09153.

Carozza, D. A., L. A. Mysak, and G. A. Schmidt (2011), Methane and environmental change during the Paleocene-Eocene Thermal maximum (PETM): Modeling the PETM onset as a two-stage event, *Geophys. Res. Lett.*, *38*, L05702, doi:10.1029/2010GL046038.

Carslaw, H. S., and J. C. Jaeger (1959), *Conduction of Heat in Solids*, Oxford University Press, Oxford.

Catling, D. C., M. W. Claire, and K. J. Zahnle (2007), Anaerobic methanotrophy and the rise of atmospheric oxygen, *Royal Soc. London Phil. Trans. A*, *365*, 1867–1888, doi:10.1098/rsta.2007.2047.

Charles, A. J., D. J. Condon, I. C. Harding, H. Pälike, J. E. A. Marshall, Y. Cui, L. Kump, and I. W. Croudace (2011), Constraints on the numerical age of the Paleocene-Eocene boundary, *Geochem. Geophys. Geosys.*, *12*, Q0AA17, doi:10.1029/2010GC003426.

Chun, C. O. J., M. L. Delaney, and J. C. Zachos (2010), Paleoredox changes across the Paleocene-Eocene thermal maximum, Walvis Ridge (ODP Sites 1262, 1263, and 1266): Evidence from Mn and U enrichment factors, *Paleoceanography*, *25*, PA4202, doi:10.1029/2009PA001861.

Crank, J., and P. Nicolson (1947), A practical method for numerical evaluation of solutions of partial differential equations of the heat-conduction type, *Math. Proc. Cambridge Phil. Soc.*, *43*, 50–67, doi:10.1017/S0305004100023197.

Cui, Y., L. R. Kump, A. J. Ridgwell, A. J. Charles, C. K. Junium, A. F. Diefendorf, K. H. Freeman, N. M. Urban, and I. C. Harding (2011), Slow release of fossil carbon during the Palaeocene-Eocene Thermal Maximum, *Nature Geosci.*, *4*, 481–485, doi:10.1038/ngeo1179.

Cui, Y., L. R. Kump, A. J. Ridgwell, A. J. Charles, C. K. Junium, A. F. Diefendorf, K. H. Freeman, N. M. Urban, and I. C. Harding (2012), Constraints on hyperthermals. Reply to comment on "Slow release of fossil carbon during the Palaeocene-Eocene Thermal Maximum", by Cui et al., 2011 Nature Geoscience, *Nature Geosci.*, *5*, 231–232.

Dickens, G. R. (2000), Methane oxidation during the late Palaeocene Thermal Maximum, *Bull. Soc. Geol. France*, *171*(1), 37–49.

Dickens, G. R. (2003), Rethinking the global carbon cycle with a large, dynamic and microbially mediated gas hydrate capacitor, *Earth Planet. Sci. Lett.*, *213*, 169–183.

Dickens, G. R. (2011), Down the Rabbit Hole: Toward appropriate discussion of methane release from gas hydrate systems during the Paleocene-Eocene thermal maximum and other past hyperthermal events, *Clim. Past*, *7*, 831–846, doi:10.5194/cp-7-831-2011.

Dickens, G. R., and M. S. Quinby-Hunt (1994), Methane hydrate stability in seawater, *Geophys. Res. Lett.*, *21*, 2115–2118, doi:10.1029/94GL01858.

Dickens, G. R., J. R. O'Neil, D. K. Rea, and R. M. Owen (1995), Dissociation of oceanic methane hydrate as a cause of the carbon isotope excursion at the end of the Paleocene, *Paleoceanogr.*, *10*, 965–971.

Dickson, A. J., A. S. Cohen, and A. L. Coe (2012), Seawater oxygenation during the Paleocene-Eocene Thermal Maximum, *Geology*, *40*(7), 639–642, doi:10.1130/G32977.1.

Divins, D. L. (2003), *Total sediment thickness of the world's oceans & marginal seas*, NOAA National Geophysical Data Center, Boulder, CO. www.ngdc.noaa.gov/mgg/sedthick.

Fantle, M. S., and D. J. DePaolo (2006), Sr isotopes and pore fluid chemistry in carbonate sediment of the Ontong Java Plateau: Calcite recrystallization rates and evidence for a rapid rise in seawater Mg over the last 10 million years, *Geochim. Cosmochim. Acta*, *70*, 3883–3904, doi:10.1016/j.gca.2006.06.009.

Farley, K. A., and S. F. Eltgroth (2003), An alternative age model for the Paleocene-Eocene thermal maximum using extraterrestrial [3]He, *Earth Planet Sci. Lett.*, *208*, 135–148.

Goldhammer, R. K. (1997), Compaction and decompaction algorithms for sedimentary carbonates, *J. Sed. Res.*, *67*(1), 26–35, doi:10.1306/-D42684E1-2B26-11D7-8648000102C1865D.

Hensen, C., M. Zabel, K. Pfeifer, T. Schwenk, S. Kasten, N. Riedinger, H. Schulz, and A. Boetius (2003), Control of sulfate pore-water profiles by sedimentary events and the significance of anaerobic oxidation of methane for the burial of sulfur in marine sediments, *Geochim. Cosmochim. Acta*, *67*, 2631–2647, doi:10.1016/S0016-7037(03)00199-6.

Hinrichs, K.-U., and A. Boetius (2002), The anaerobic oxidation of methane: New insights in microbial ecology and biogeochemistry, in *Ocean Margin Systems*, edited by Wefer, G. et al., Springer-Verlag, Berlin Heidelberg, pp. 457–477.

Jørgensen, B. B. (1977), The sulfur cycle of a coastal marine sediment (Limfjorden, Denmark), *Limnol. Oceanogr.*, *22*(5), 814–832.

Jørgensen, B. B., and S. Kasten (2006), Sulfur cycling and methane oxidation, in *Marine Geochemistry*, edited by H. Schulz, and M. Zabel, pp. 271–309, Springer, Berlin Heidelberg. doi: 10.1007/3-540-32144-6_8.

Jørgensen, B. B., M. E. Böttcher, H. Lüschen, L. N. Neretin, and I. I. Volkov (2004), Anaerobic methane oxidation and a deep H_2S sink generate isotopically heavy sulfides in Black Sea sediments, *Geochim. Cosmochim. Acta*, *68*, 2095–2118, doi:10.1016/j.gca.2003.07.017.

Joye, S. B., et al. (2011), Comment on "A persistent oxygen anomaly reveals the fate of spilled methane in the Deep Gulf of Mexico", *Science*, *332*, 1033, doi:10.1126/science.1203307.

Katz, M. E., B. S. Cramer, G. S. Mountain, S. Katz, and K. G. Miller (2001), Uncorking the bottle: What triggered the Paleocene/Eocene thermal maximum methane release? *Paleoceanography*, *16*, 549–562, doi:10.1029/2000PA000615.

Kennett, J. P., and L. D. Stott (1991), Abrupt deep-sea warming, palaeoceanographic changes and benthic extinctions at the end of the Palaeocene, *Nature*, *353*, 225–229.

Kessler, J. D., et al. (2011), A persistent oxygen anomaly reveals the fate of spilled methane in the deep Gulf of Mexico, *Science*, *331*, 312–315, doi:10.1126/science.1199697.

Koch, P. L., J. C. Zachos, and P. D. Gingerich (1992), Correlation between isotope records in marine and continental carbon reservoirs near the Paleocene/Eocene boundary, *Nature*, *358*, 319–322, doi:10.1038/358319a0.

Krumins, V., M. Gehlen, S. Arndt, P. Van Cappellen, and P. Regnier (2013), Dissolved inorganic carbon and alkalinity fluxes from coastal marine sediments: Model estimates for different shelf environments and sensitivity to global change, *Biogeosciences*, *10*, 371–398, doi:10.5194/bg-10-371-2013.

Kwon, E. Y., F. Primeau, and J. L. Sarmiento (2009), The impact of remineralization depth on the air-sea carbon balance, *Nature Geosci.*, *2*, 630–635, doi:10.1038/ngeo612.

Lourens, L. J., A. Sluijs, D. Kroon, J. C. Zachos, E. Thomas, U. Röhl, J. Bowles, and I. Raffi (2005), Astronomical pacing of late Palaeocene to early Eocene global warming events, *Nature*, *435*, 1083–1087, doi:10.1038/nature03814.

Malinverno, A., and J. W. Pohlman (2011), Modeling sulfate reduction in methane hydrate-bearing continental margin sediments: Does a sulfate-methane transition require anaerobic oxidation of methane? *Geochem. Geophys. Geosys.*, *12*, Q07006, doi:10.1029/2011GC003501.

Matsumoto, K. (2007), Biology-mediated temperature control on atmospheric pCO_2 and ocean biogeochemistry, *Geophys. Res. Lett.*, *34*, L20605, doi:10.1029/2007GL031301.

Morin, R. H., and R. P. von Herzen (1986), Geothermal measurements at Deep Sea Drilling Project Site 587, in *Initial Reports of the Deep Sea Drilling Project*, edited by Kennett, J. P. et al., U.S. Govt. Printing Office, Washington, pp. 1317–1324.

Murphy, B. H., K. A. Farley, and J. C. Zachos (2010), An extraterrestrial [3]He-based timescale for the Paleocene-Eocene thermal maximum (PETM) from Walvis Ridge, IODP Site 1266, *Geochim. Cosmochim. Acta*, *74*, 5098–5108, doi:10.1016/j.gca.2010.03.039.

Paull, C. K., T. Lorenson, W. Borowski, W. I. Ussler, K. Olsen, and N. Rodriguez (2000), Isotopic composition of CH_4, CO_2 species, and sedimentary organic matter within samples from the Blake Ridge: Gas source implications, in *Proc. ODP, Sci. Res.*, edited by Paull, C. K.

et al., vol. 164, Ocean Drilling Program, College Station, TX, pp: 67–78. www.odp.tamu.edu.

Penman, D. E., J. C. Zachos, R. E. Zeebe, B. Hönisch, and S. Bohaty (2011), B/Ca of planktic foraminifera documents elevated pCO_2 and ocean acidification during the Paleocene-Eocene Thermal Maximum. *AGU Fall Meet. 2011*, PP21E–07.

Press, W. H., B. P. Flannery, S. A. Teukolsky, and W. T. Vetterling (1992), *Numerical Recipes in C: The Art of Scientific Computing*, pp. 1020, Cambridge University, Cambridge.

Reeburgh, W. S., S. C. Whalen, and M. J. Alperin (1993), The role of methylotrophy in the global methane budget, in *Microbial Growth on C-1 compounds*, edited by J. C. Murrel, and D. P. Kelly, Kluwer Academic Publishers, Kluwerhagen, 1–14.

Rempel, A. W., and B. A. Buffett (1997), Formation and accumulation of gas hydrate in porous media, *J. Geophys. Res.*, *102*(B5), 10,151–10,164, doi:10.1029/97JB00392.

Richter, F. M. (1993), Fluid flow in deep-sea carbonates: Estimates based on porewater SR, *Earth Planet. Sci. Lett.*, *119*, 133-141.

Robertson, E. C. (1988), *Thermal Properties of Rocks*, U.S. Dept. of the Interior, Geological Survey, Denver, CO. pubs.usgs.gov/of-1988/0441/report.pdf.

Röhl, U., T. Westerhold, T. J. Bralower, and J. C. Zachos (2007), On the duration of the Paleocene-Eocene thermal maximum (PETM), *Geochem. Geophys. Geosyst.*, *8*, Q12002, doi:10.1029/2007GC001784.

Schmidt, G. A., and D. T. Shindell (2003), Atmospheric composition, radiative forcing, and climate change as a consequence of a massive methane release from gas hydrates, *Paleoceanography*, *18*(1), 1004, doi:10.1029/2002PA000757.

Sluijs, A., et al. (2006), Subtropical Arctic Ocean temperatures during the Palaeocene/Eocene thermal maximum, *Nature*, *441*, 610–613.

Sluijs, A., J. C. Zachos, and R. E. Zeebe (2012), Constraints on hyperthermals. Comment on "Slow release of fossil carbon during the Palaeocene-Eocene Thermal Maximum", by Cui et al., 2011 Nature Geoscience, *Nature Geosci.*, *5*, 231.

Tripati, A., and H. Elderfield (2005), Deep-sea temperature and circulation changes at the Paleocene-Eocene Thermal Maximum, *Science*, *308*, 1894–1898.

Turchyn, A. V., and D. P. Schrag (2006), Cenozoic evolution of the sulfur cycle: Insight from oxygen isotopes in marine sulfate, *Earth Planet. Sci. Lett.*, *241*, 763–779, doi:10.1016/j.epsl.2005.11.007.

Valentine, D. L. (2002), Biogeochemistry and microbial ecology of methane oxidation in anoxic environments: A review, *Antonie van Leeuwenhoek*, *81*(1-4), 271–282, doi:10.1023/A:1020587206351.

Von Herzen, R., and A. E. Maxwell (1959), The measurement of thermal conductivity of deep-sea sediments by a needle-probe method, *J. Geophys. Res.*, *64*(10), 1557–1563, doi:10.1029/JZ064i010p01557.

Vosteen, H., and R. Schellschmidt (2003), Influence of temperature on thermal conductivity, thermal capacity and thermal diffusivity for different types of rock, *Phys. Chem. Earth*, *28*, 499–509, doi:10.1016/S1474-7065(03)00069-X.

Wolf-Gladrow, D. A., R. E. Zeebe, C. Klaas, A. Körtzinger, and A. G. Dickson (2007), Total alkalinity: The explicit conservative expression and its application to biogeochemical processes, *Mar. Chem.*, *106*, 287–300.

Xu, W., R. P. Lowell, and E. T. Peltzer (2001), Effect of seafloor temperature and pressure variations on methane flux from a gas hydrate layer: Comparison between current and late Paleocene climate conditions, *J. Geophys. Res.*, *106*(B11), 26,413–26,423, doi:10.1029/2001JB000420.

Zachos, J. C., M. Pagani, L. Sloan, E. Thomas, and K. Billups (2001), Trends, rhythms, and aberrations in global climate 65 Ma to present, *Science*, *292*, 686–693.

Zachos, J. C., M. W. Wara, S. M. Bohaty, M. L. Delaney, M. Rose-Petrizzo, A. Brill, T. J. Bralower, and I. Premoli-Silva (2003), A transient rise in tropical sea surface temperature during the Paleocene-Eocene Thermal Maximum, *Science*, *302*, 1551–1554.

Zachos, J. C., et al. (2005), Rapid acidification of the ocean during the Paleocene-Eocene Thermal Maximum, *Science*, *308*, 1611–1615.

Zeebe, R. E. (2007), Modeling CO_2 chemistry, δ^{13}C, and oxidation of organic carbon and methane in sediment porewater: Implications for paleo-proxies in benthic foraminifera, *Geochim. Cosmochim. Acta*, *71*, 3238–3256.

Zeebe, R. E. (2012), LOSCAR: Long-term Ocean-atmosphere-Sediment CArbon cycle Reservoir Model v2.0.4, *Geosci. Model Dev.*, *5*, 149–166.

Zeebe, R. E., and D. A. Wolf-Gladrow (2001), *CO_2 in Seawater: Equilibrium, Kinetics, Isotopes*, pp. 346., Elsevier Oceanography Series, Amsterdam.

Zeebe, R. E., and J. C. Zachos (2013), Long-term legacy of massive carbon input to the Earth system: Anthropocene vs. Eocene, *Royal Soc. London Phil. Trans. A*, *371*(29), doi:10.1098/rsta.2012.0006.

Zeebe, R. E., J. C. Zachos, and G. R. Dickens (2009), Carbon dioxide forcing alone insufficient to explain Palaeocene-Eocene Thermal Maximum warming, *Nature Geosci.*, *2*, 576–580, doi:10.1038/ngeo578.